Supporting Information

Impact of Halide Alloying on the Phase Segregation of Mixed-Halide Perovskites

*Joshua R. S. Lilly, Vincent J.-Y. Lim, Jay B. Patel, Siyu Yan, Jae Eun Lee, Michael B. Johnston, Laura M. Herz**

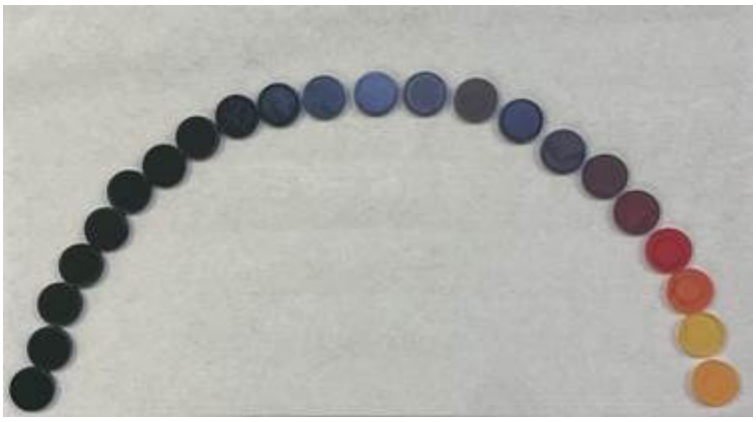

Figure S1. Image of $MAPb(I_{1-x}Br_x)_3$ thin films on z-cut quartz substrates. From left to right, the nominal bromide fraction was: 0, 0.1, 0.15, 0.2, 0.25, 0.3, 0.333, 0.4, 0.425, 0.45, 0.475, 0.5, 0.525, 0.55, 0.575, 0.6, 0.667, 0.7, 0.8, 0.83, 0.9, and 1.

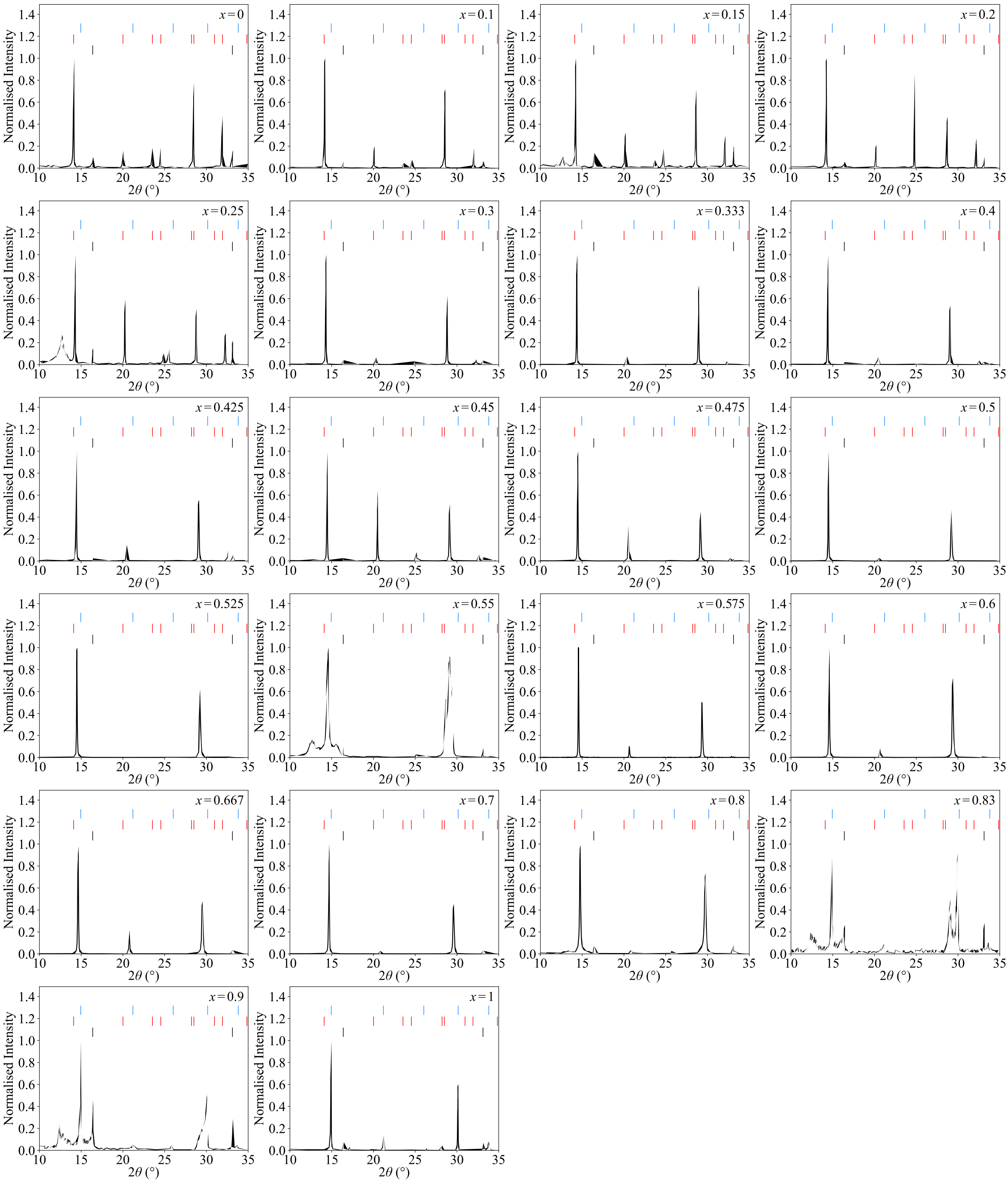

Figure S2. X-ray diffraction patterns for $MAPb(I_{1-x}Br_x)_3$ thin films on z-cut quartz substrates. Films were not encapsulated. Diffraction patterns were recorded using monochromatic Cu-Kα_1 radiation. The nominal bromide fraction is indicated in the upper-right of each individual plot. Characteristic substrate diffraction peaks are evident at 16.4 ° and 33.1 ° (the (001) and (002) reflections are highlighted in the black stick plots).[1,2] Reference stick plots for $MAPbI_3$ are presented in red, with the (002)/(110), (112)/(200), (211), (202), (004), (220), (213), (114)/(222)/(310), and (204)/(312) reflections highlighted (with the slash noting reflections that are overlapping).[3] Reference stick plots for $MAPbBr_3$ are presented in blue, with the (100), (110), (111), (200), and (210) reflections highlighted.[4]

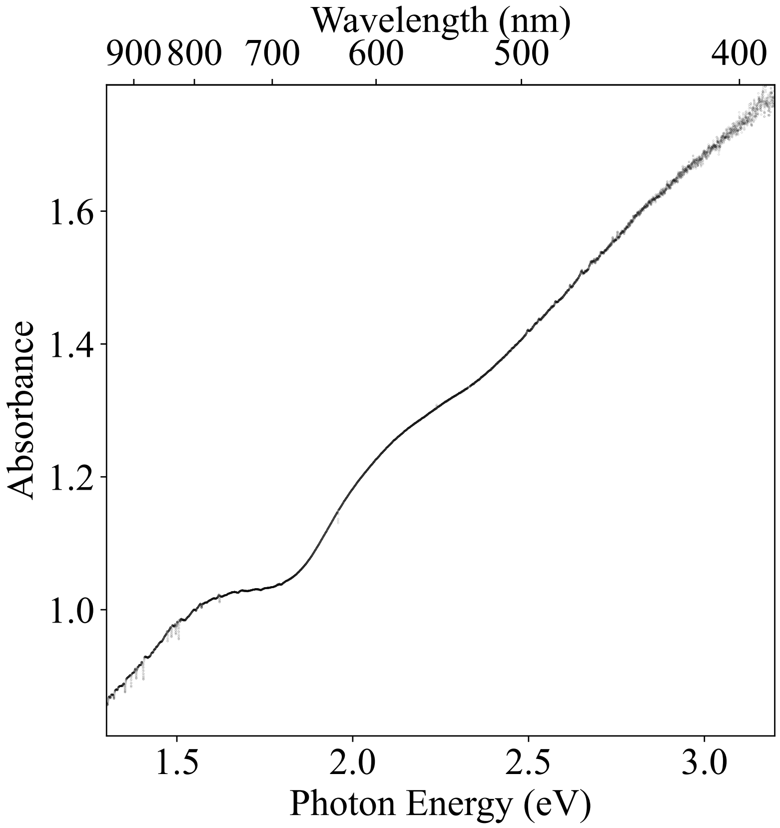

Figure S3. Absorbance spectra of the MAPb($I_{1-x}Br_x$)$_3$ thin film with a nominal bromide fraction of $x = 0.55$. Note the broad nature of the absorption onset,[5] indicative of poor compositional homogeneity.

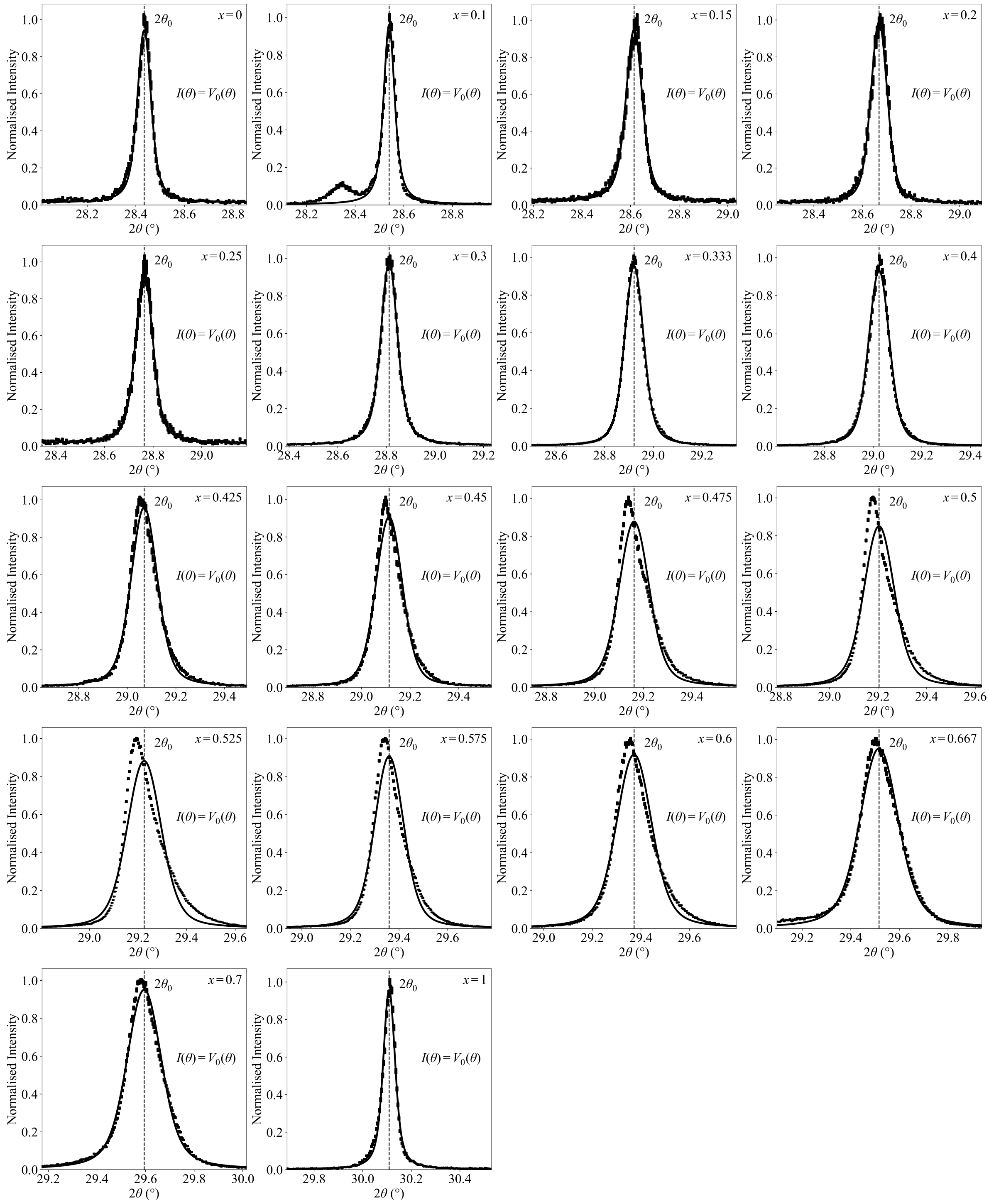

Figure S4. Second-order diffraction peak for $MAPb(I_{1-x}Br_x)_3$ thin films on z-cut quartz substrates. Films were not encapsulated. Diffraction patterns were recorded using monochromatic Cu-Kα_1 radiation. The nominal bromide fraction is indicated in the upper-right of each individual plot. Data is modelled with a single Voigt profile. The dashed line indicates the peak centre extracted from the fit, and is marked as $2\theta_0$. Note, for nominal bromide fractions of less than 0.15, (220) and (004) reflections are expected to be present (their relative amplitude dependent on texturing), consistent with the tetragonal (β) phase.[6,7]

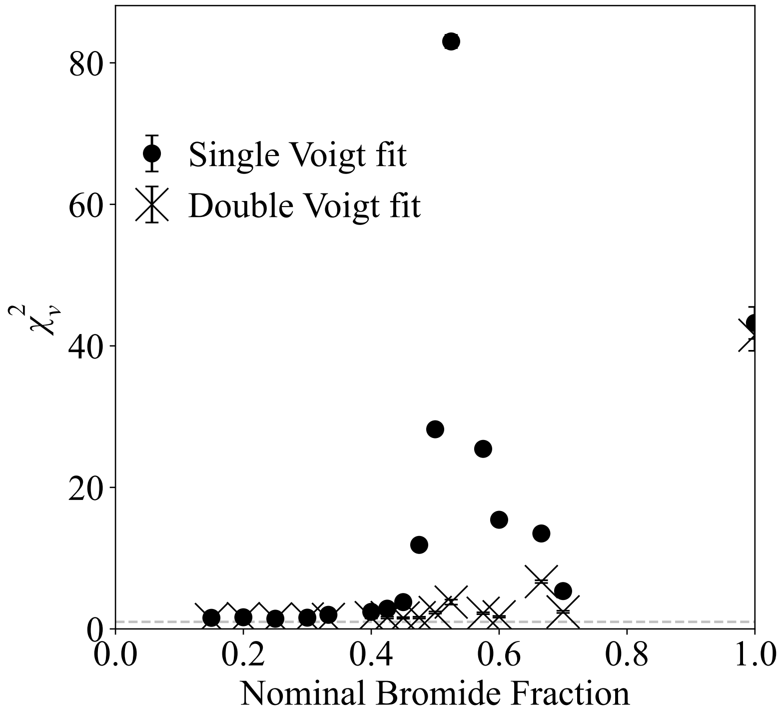

Figure S5. Minimised reduced χ^2 (χ_v^2) when either a single Voigt profile (filled circles) or the sum of two Voigt profiles (crosses) are used to model the (200) diffraction peak. Compositions that crystallised into the tetragonal phase (i.e., $x = 0$ and $x = 0.1$) have been omitted. The χ_v^2 for $MAPbBr_3$ is significantly impacted by a small secondary peak (located at approximately 28.2 °) being included in the range of the χ_v^2 calculation (see Figure S6). To ensure generality in the analysis, it was decided that the same calculation range should be used for all compositions. As can be seen in Figure S4 and Figure S9, this secondary peak does not influence the fitting of the (200) diffraction peak, and the relative improvement in χ_v^2 is found to be approximately unity (Figure 1d).

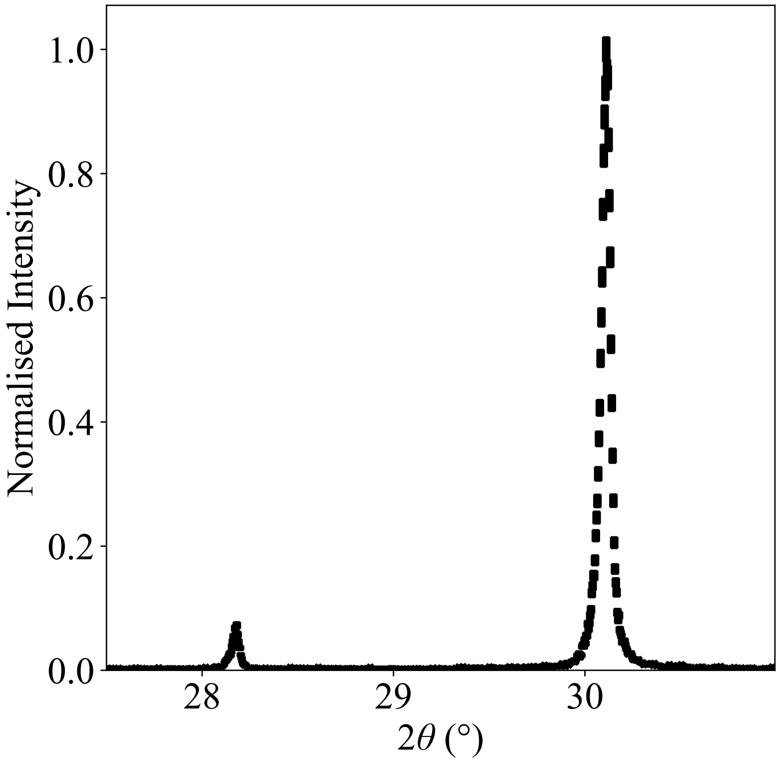

Figure S6. Second-order diffraction peak for a $MAPbBr_3$ thin film. The film was not encapsulated. The diffraction pattern was recorded using monochromatic Cu-Kα_1 radiation. Note the small secondary peak at approximately 28.2 ° that influenced the χ_υ^2 calculation.

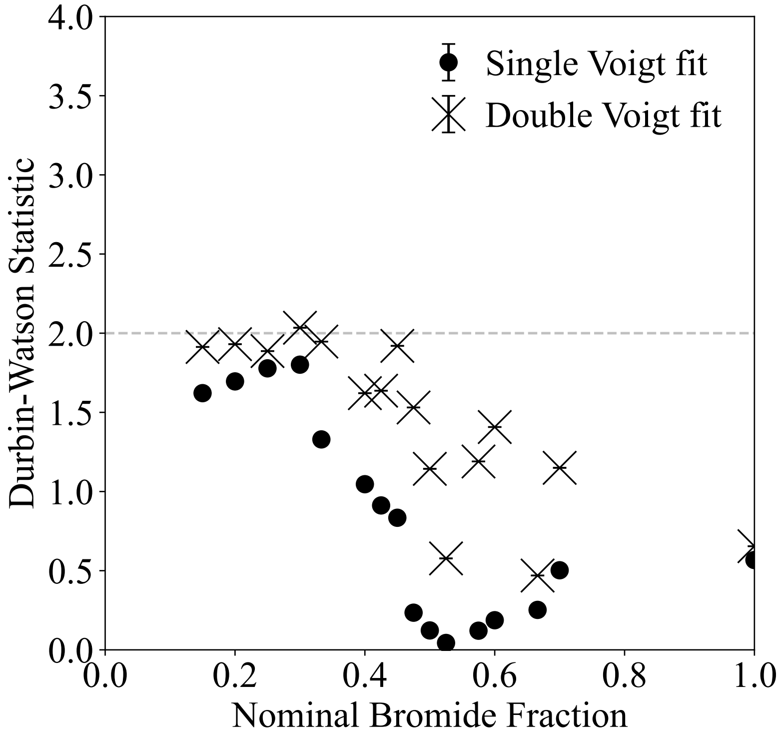

Figure S7. Durbin-Watson statistic for the two cases of using a single Voigt profile (filled circles) and the sum of two Voigt profiles (crosses) to model the (200) diffraction peak. Compositions that crystallised into the tetragonal phase (i.e., x = 0 and x = 0.1) have been omitted. The associated Durbin-Watson statistic for $MAPbBr_3$ is significantly impacted by a small secondary peak (located at approximately 28.2 °) being included in the range of the calculation (see Figure S6). To ensure generality in the analysis, it was decided that the same calculation range should be used for all compositions. As can be seen in Figure S4 and Figure S9, this secondary peak does not influence the fitting of the (200) diffraction peak, and the relative improvement in the Durbin-Watson statistic is found to be approximately zero (Figure S8).

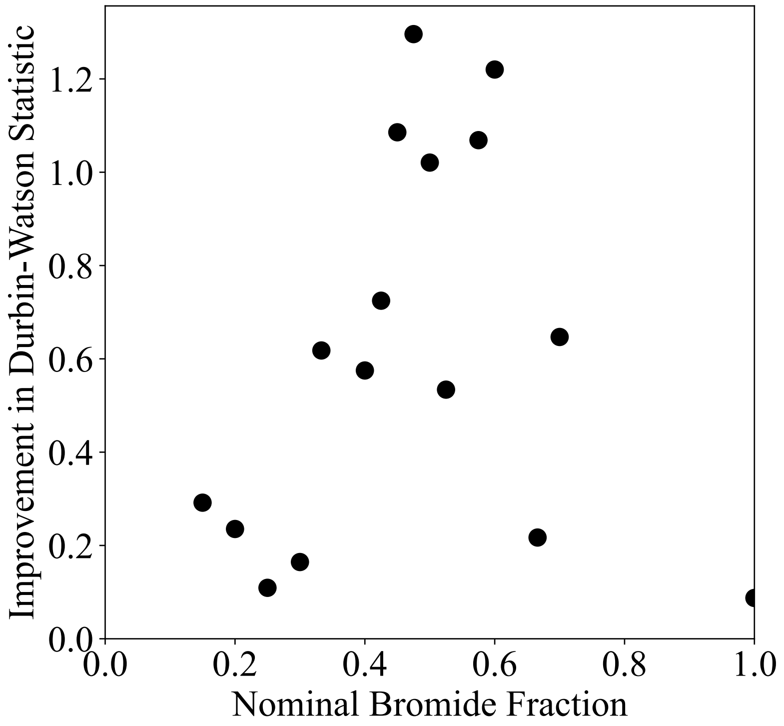

Figure S8. Improvement in the Durbin-Watson statistic (i.e., how much closer to the ideal value of two) when moving from fits based on a single Voigt profile to those based on the sum of two Voigt profiles to model the (200) diffraction peak. Compositions that crystallised into the tetragonal phase (i.e., $x = 0$ and $x = 0.1$) have been omitted.

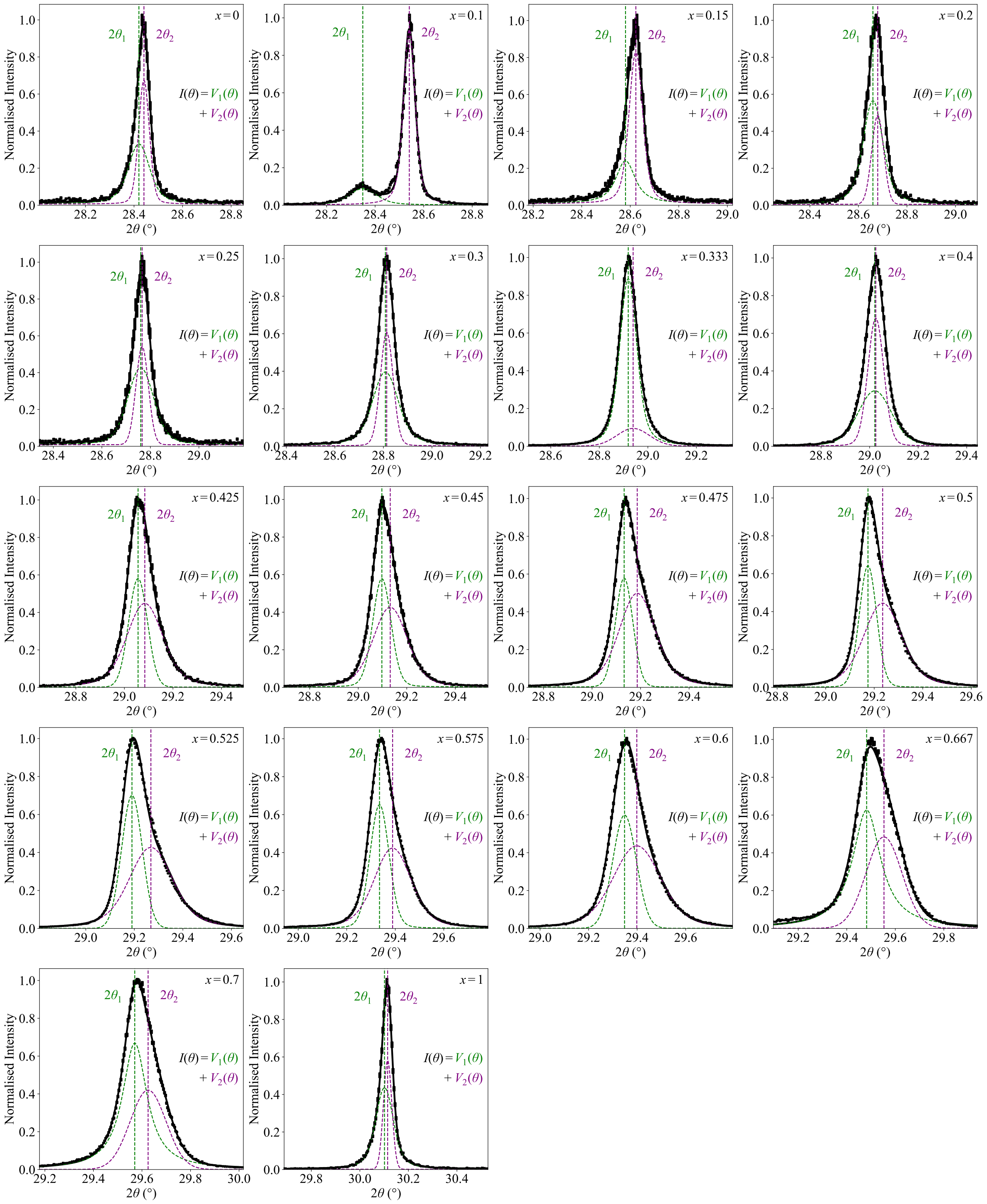

Figure S9. Second-order diffraction peak for $MAPb(I_{1-x}Br_x)_3$ thin films. Films were not encapsulated. Diffraction patterns were recorded using monochromatic Cu-Kα_1 radiation. The nominal bromide fraction is indicated in the upper-right of each individual plot. Data (signal intensity, I) is modelled with the sum of two Voigt profiles (V_1 and V_2). The dashed lines indicate the peak centres ($2\theta_1$ and $2\theta_2$) extracted from the fit.

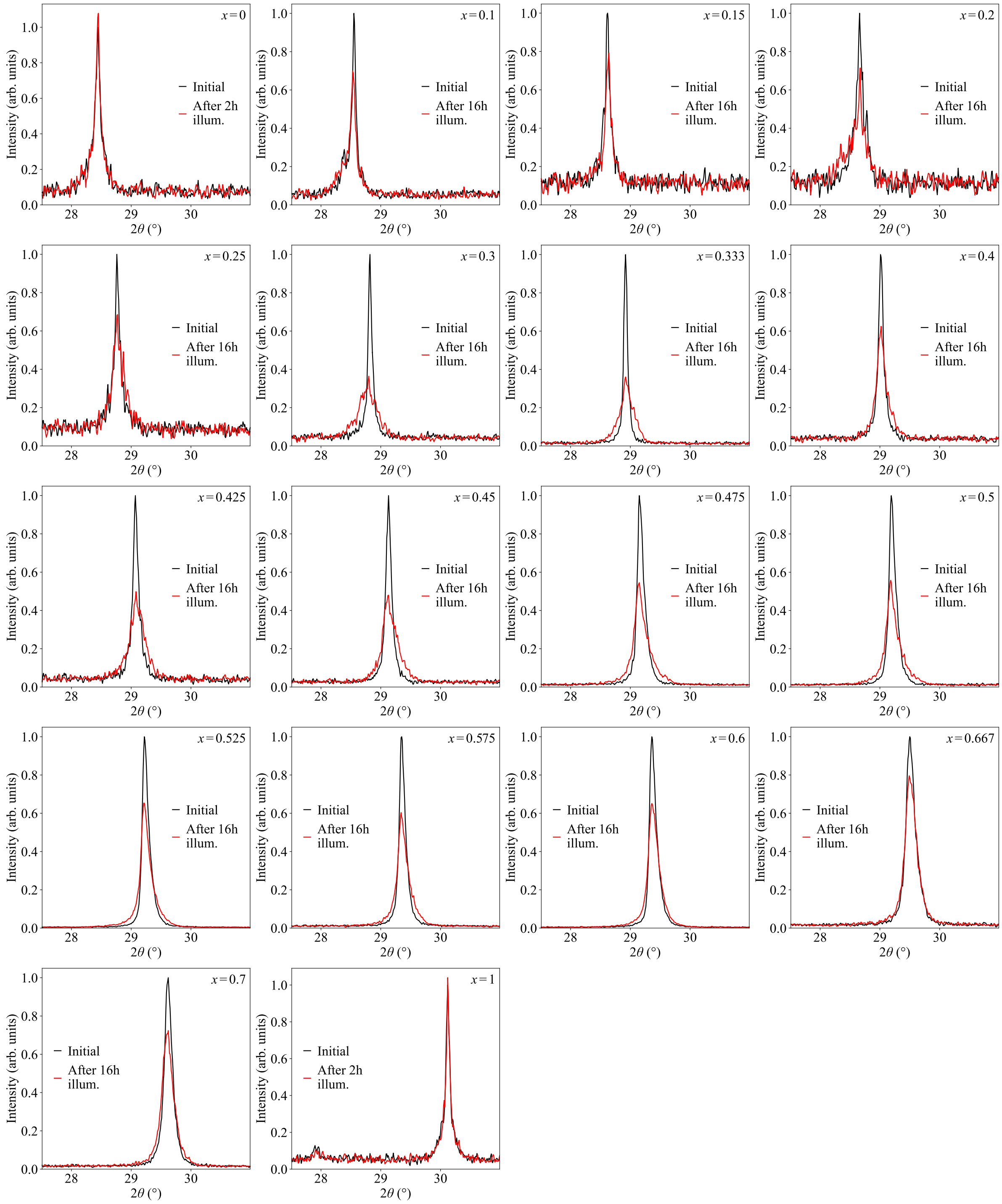

Figure S10. Second-order diffraction peak for $MAPb(I_{1-x}Br_x)_3$ thin films before (black) and after (red) 16 h of illumination with a constant intensity of 0.91 mWcm^{-2} via a 470 nm continuous wave laser excitation. Note, single-halide compositions ($MAPbI_3$ and $MAPbBr_3$) were only light-soaked for two hours, as they cannot be susceptible to halide segregation. Films were encapsulated. Diffraction patterns were recorded using monochromatic Cu-Kα_1 radiation. The nominal bromide fraction is indicated in the upper-right of each individual plot.

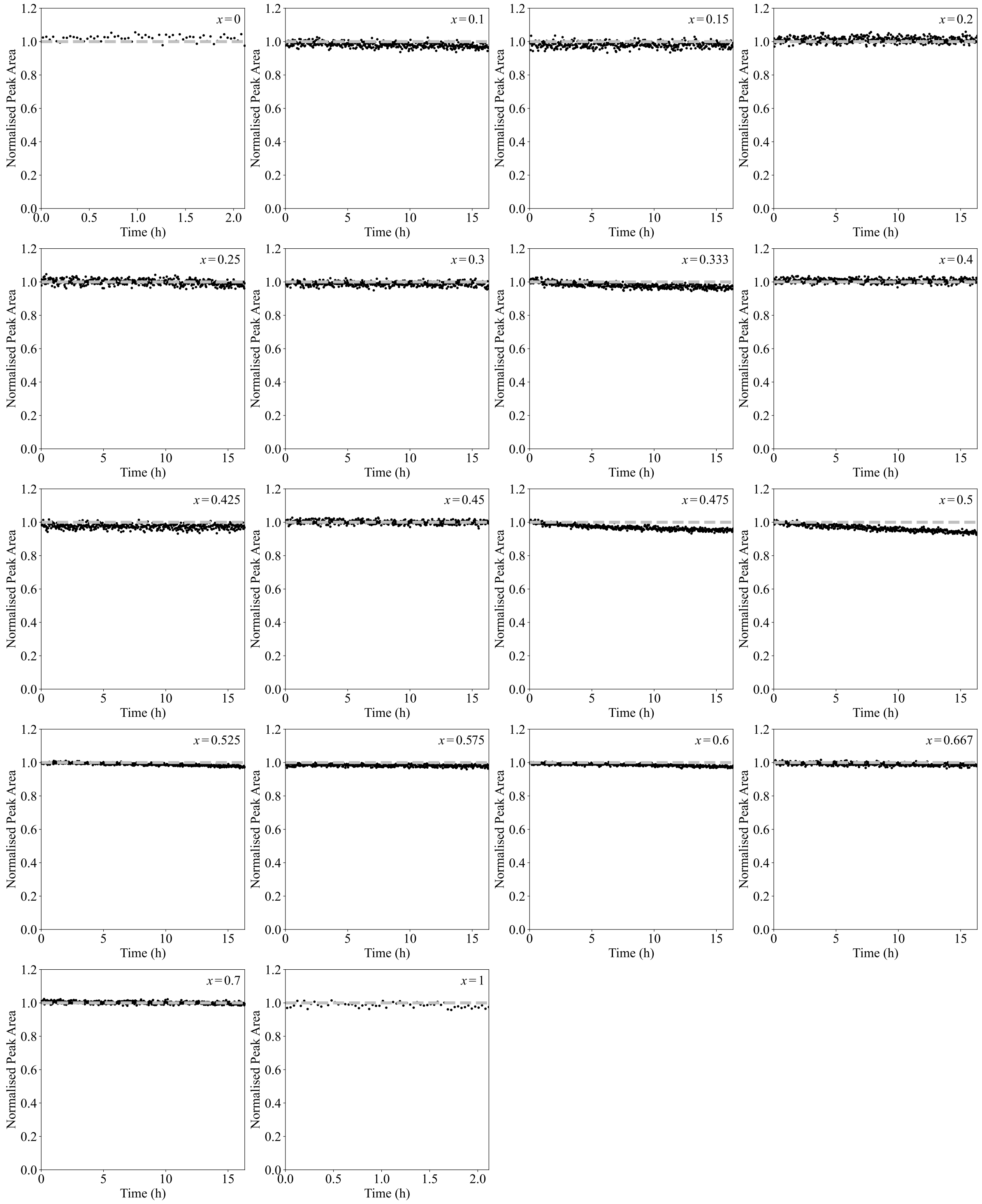

Figure S11. Area underneath the second-order diffraction peak for MAPb(I$_{1-x}$Br$_x$)$_3$ thin films normalised to the initial peak area. Films were encapsulated with PMMA and illuminated with a constant intensity of 0.91 mWcm^{-2} via 470 nm continuous wave laser excitation. Note, single-halide compositions (MAPbI$_3$ and MAPbBr$_3$) were only light-soaked for two hours, as they cannot be susceptible to halide segregation. The nominal bromide fraction is indicated in the upper-right of each individual plot.

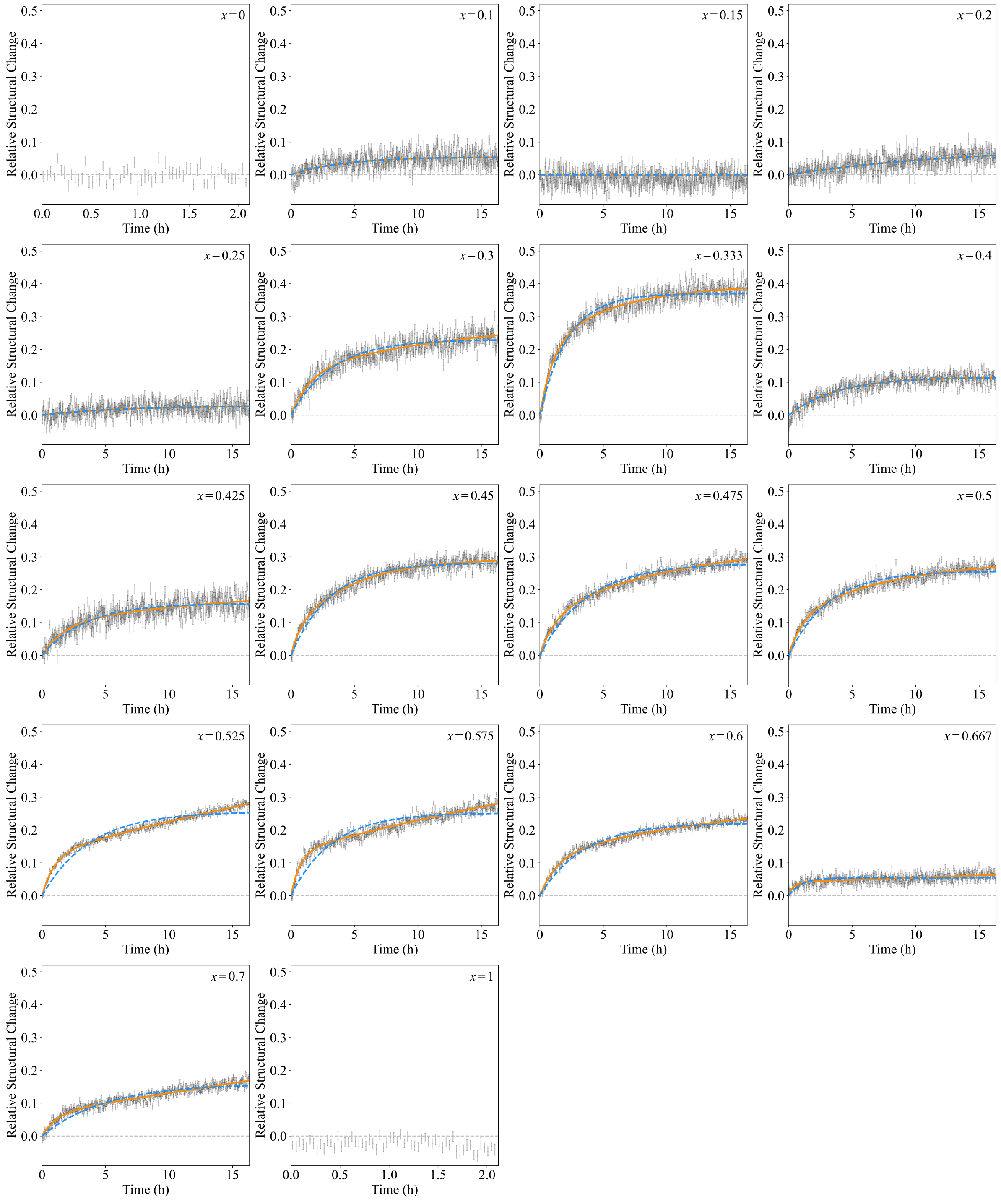

Figure S12. Relative structural change in thin films of MAPb($I_{1-x}Br_x$)$_3$ arising from halide segregation. The relative structural change is calculated by taking the absolute integral of the differential X-ray diffraction intensity (grey shading, Figure 2b), and normalising with respect to the time-zero diffraction profile (further details in Supporting Note 3). Films were encapsulated and illuminated with a constant intensity of 0.91 mWcm^{-2} via 470 nm continuous wave laser excitation. The result of the model fitting for a monoexponential and a biexponential function are plotted in blue and orange respectively. Data for $MAPbI_3$ and $MAPbBr_3$ were not modelled. The nominal bromide fraction is indicated in the upper-right of each individual plot.

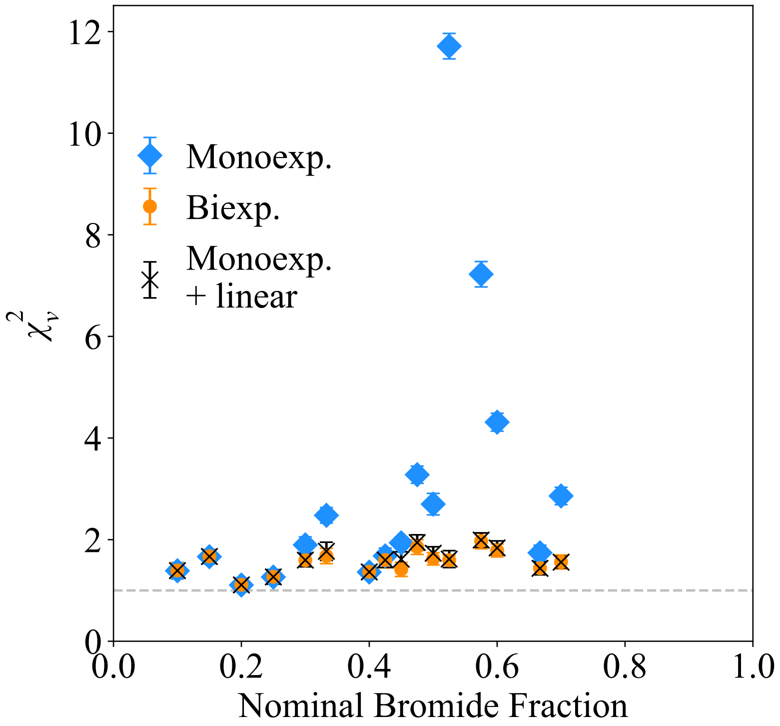

Figure S13. Reduced minimised χ^2 (χ_v^2) for the three cases of using a monoexponential function, a biexponential function, and the sum of a monoexponential function and a linear function (constrained to go through the origin) to model the relative structural change.

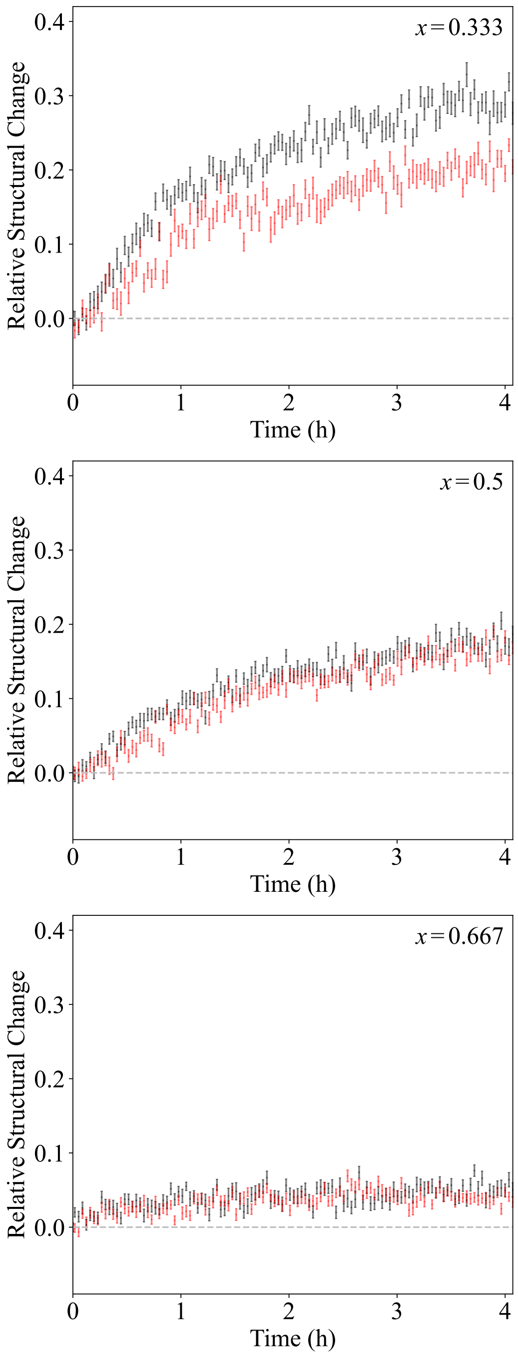

Figure S14. Relative structural change as a function of illumination time, extracted for two different $MAPb(I_{1-x}Br_x)_3$ thin-film samples (red and black) of the same nominal bromide content x, evidencing minimal sample-to-sample variation for identical composition. Films were measured under identical conditions. The nominal bromide fraction is indicated in the upper-right of each individual plot.

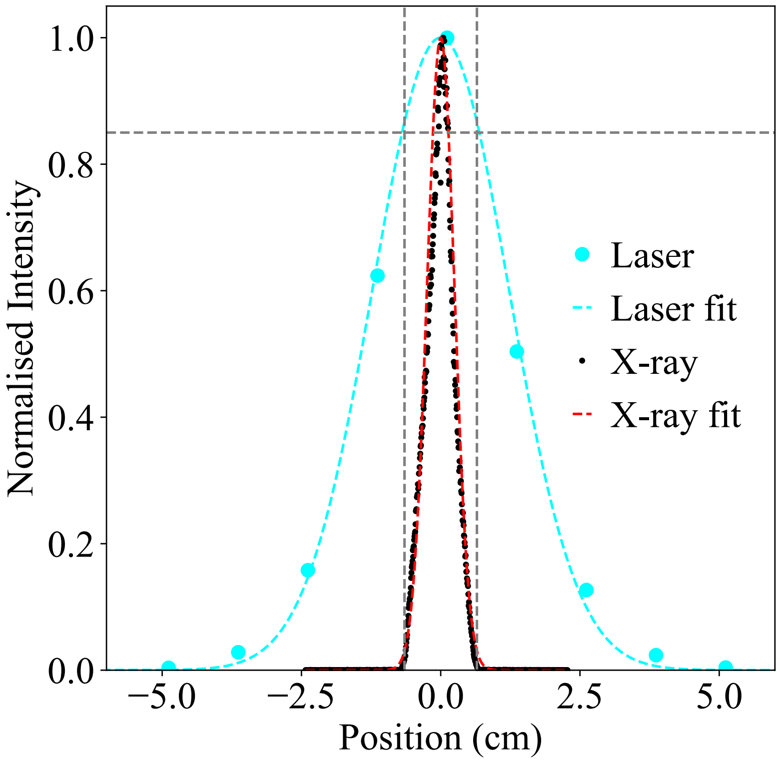

Figure S15. Horizontal profile of the X-ray beam (black, with Gaussian fit in red) at the sample position, calibrated by using a beam block of known size. Laser profile (blue circles) fit with a Gaussian function (blue dashed line). The laser excitation was incident at 45° to the normal of the thin film, resulting in an elliptical (projected) beam shape. The laser profile shown is that taken along the minor elliptical axis, and is thus representative of the maximal possible excitation variation across the sample surface. Vertical dashed grey lines highlight the extent of the sample. The dashed grey horizontal line signifies an intensity reduction of 15% compared to that at the centre of the optical excitation. As indicated, there is minimal variation (< 15%) in the local optical illumination intensity across the extent of the sample.

Bromide fraction (x)	Macrostrained phases	Segregation extent	Segregation rate	Impact of halide ordering on segregation	Notes on device applicability
0	No evidence	Does not segregate			N/A
0.1			The rate of halide segregation is broadly constant across the entire range of halide ratios investigated	N/A	Be aware that segregation can still occur for $x < 0.2$
0.15					
0.2					
0.25					N/A
0.3					
1/3		More seg. than Gaussian baseline		Particularly photo-unstable	Avoid using in Si-MHP tandems
0.4		Follows a Gaussian-like distribution that is symmetric and centred close to a bromide fraction of 0.5		N/A	N/A
0.425	Limited evidence				Strain engineering could be utilised to enhance the stability of top cells in all-perovskite 2J and silicon-MHP-MHP 3J
0.45					
0.475	Strong evidence of macrostrained phases with the difference in macrostrain maximising near $x = 0.5$				
0.5					
0.525					
0.575					
0.6					
2/3	Limited evidence	Less seg. than Gaussian baseline		Particularly photostable	Use for top cell in all-perovskite 3J
0.7				N/A	N/A
1	No evidence	Does not segregate			

Table S1. Table summarising the results of the study and proposed design strategies to enhance the stability of different multi-junction perovskite-based solar cell architectures.

Supporting Note 1: Further discussion of diffraction peak asymmetry

The (200) diffraction peak was selected for analysis in order to maximise angular resolution, whilst retaining sufficient signal intensity.[8] As the asymmetry is present as a high-angle tail (rather than a low-angle tail), axial divergence can be ruled out as the cause of this asymmetry.[9,10] Further, as a monochromatic probe is being utilised (Cu-Kα_1), beam non-monochromaticity can additionally be excluded. Diffraction experiments on unencapsulated films began 18 days after initial deposition, with experiments occurring over four consecutive days. Films were removed from the glovebox in small groups for measurement (between one and three samples), with each XRD scan lasting approximately 30 minutes. Films were measured in the order of increasing bromide fraction, ruling out any time-dependent bias on the formation of an asymmetric peak. Our observations were consistent across samples batches (Figure S16), across different X-ray diffractometers (Figure S17 and Figure S18), and were independent of whether films were or were not encapsulated with PMMA immediately after MHP deposition (Figure S19 and Figure S20) – reinforcing the consistency of our results.

MHP structures in the tetragonal phase with no strong preferential orientation should exhibit prominent (112)/(200), (211), and (202) diffraction peaks.[11] We note that the two resolved peaks, Figure 1c, are of comparable intensity. However, no prominent (112)/(200), (211), or (202) diffraction peaks are consistently identified for the compositions showing peak asymmetry (Fig. S2). Therefore, via proof by contradiction, the two lattice parameters required to describe the material structure for compositions with a nominal bromide fraction, x, close to 0.5 are not the result of a tetragonal crystalline arrangement of a single phase, but are rather due to the co-existence of two distinct material phases with different lattice parameter.

If a true miscibility gap were being observed, causing two-phases to form for immiscible compositions, one would expect clear compositional termination points for miscibility; these defined compositional turning points would be described by a fixed lattice parameter, which would lead to diffraction at a characteristic 2θ angle. This would result in an apparent peak 'gap' where, for a given 2θ range, no XRD peak positions are identified when considering diffraction spectra across the compositional series. Figure S21 shows that no distinct compositional termination points are identified.

Halide inhomogeneity has been observed previously in metal-halide perovskites.[12–14] However, Elmelund *et al.* demonstrated that halide ions can readily diffuse through the perovskite structure to achieve full entropic mixing (even overcoming terminated surfaces), with temperature greatly hastening this process.[15] Increased thermal annealing showed no meaningful change to the observed peak asymmetry, Figure S16 and Figure S22. Furthermore, diffraction spectra were further recorded after storage for approximately 8-months under ambient temperature – the observed peak asymmetry was still present (Figure S17 and Figure S18). Finally, films were light-soaked (0.91 mWcm^{-2}, as described in main text) for approximately 16 h to promote halide segregation, and allowed to re-mix in the dark for approximately 45 days; the peak asymmetry was still present after re-mixing (Figure S23 and Figure S24). Together, these results strongly evidence that the co-existence of two material phases with distinct lattice parameter for the compositional range centred around $x = 0.5$ is not caused by compositional inhomogeneity. Consequently, we suggest that the differing lattice parameters are instead due to each phase being differently strained.

Whilst microstrain results in the broadening of a diffraction peak, macrostrain manifests itself as a shift in the diffraction peak centre.[11,16] Two material phases of identical stoichiometry, but with differing macrostrain, would have slightly displaced diffraction peaks. If two such phases co-existed, the summation of these two peaks could result in an asymmetric diffraction peak profile – exactly as we have observed.

It is unlikely that the observed strain is directly induced by the substrate. The substrate utilised in this study (z-cut quartz) does not exhibit the required lattice parameters to directly lattice match $MAPb(I_{1-x}Br_x)_3$, and is thus not expected to support epitaxial growth.[17] Instead, we propose that the macrostrain identified is an intrinsic property of mixed-halide films that stabilises heavily alloyed systems against immiscibility (as similarly shown for III-V semiconductors).[18] When included in a device stack, the growth of the perovskite film will be influenced by the properties of the underlying charge transport layer.[19,20] Previous work has shown how templating layers can modulate the formation of the perovskite film,[20] and we believe that the application of such templating layers could also facilitate control of the formation of macrostrained phases of $MAPb(I_{1-x}Br_x)_3$ in device-relevant structures.

Nanostructure analysis would provide further confirmation of our observations. However, previous studies have evidenced how electron irradiation (even in an ultra-low dosage regime) can lead to ion migration and structural change.[21] Specifically, it has been found that halide segregation can be induced by an electron beam.[22] Therefore, the use of SEM/TEM would be unfeasible to categorise such nano-scale structures, as the probe itself can alter such structures. Consequently, we utilised XRD to investigate the structure, as this technique (at the laboratory scale) has been shown not to influence the material structure, even under prolonged exposure.[23] As elemental mapping via energy-dispersive X-ray spectroscopy will induce halide segregation in mixed-halide perovskites, only the nominal halide ratio (determined from precursor stoichiometry) has been utilised to designate the composition of each film. The change in diffraction peak with increasing bromide fraction (Figure S21) appears monotonic and linear (following Vegard's law), suggesting that there is no significant deviation of the actual halide ratio from the nominal halide ratio.

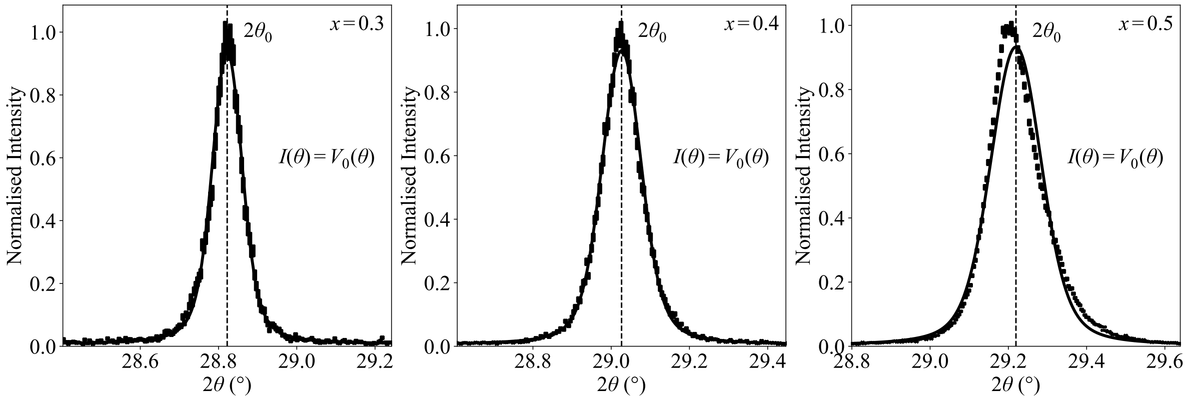

Figure S16. Second-order diffraction peak for three $MAPb(I_{1-x}Br_x)_3$ thin films of different nominal bromide fraction x, prepared as part of a separate batch (the first batch, fabricated alongside the sample set presented in Figure S22) – the same trend is observed as in Figure S4. Films were encapsulated with PMMA. Diffraction patterns were recorded using monochromatic Cu-Kα_1 radiation. The nominal bromide fraction is indicated in the upper-right of each individual plot. Data is modelled with a single Voigt profile. The dashed line indicates the peak centre extracted from the fit, and is marked as $2\theta_0$.

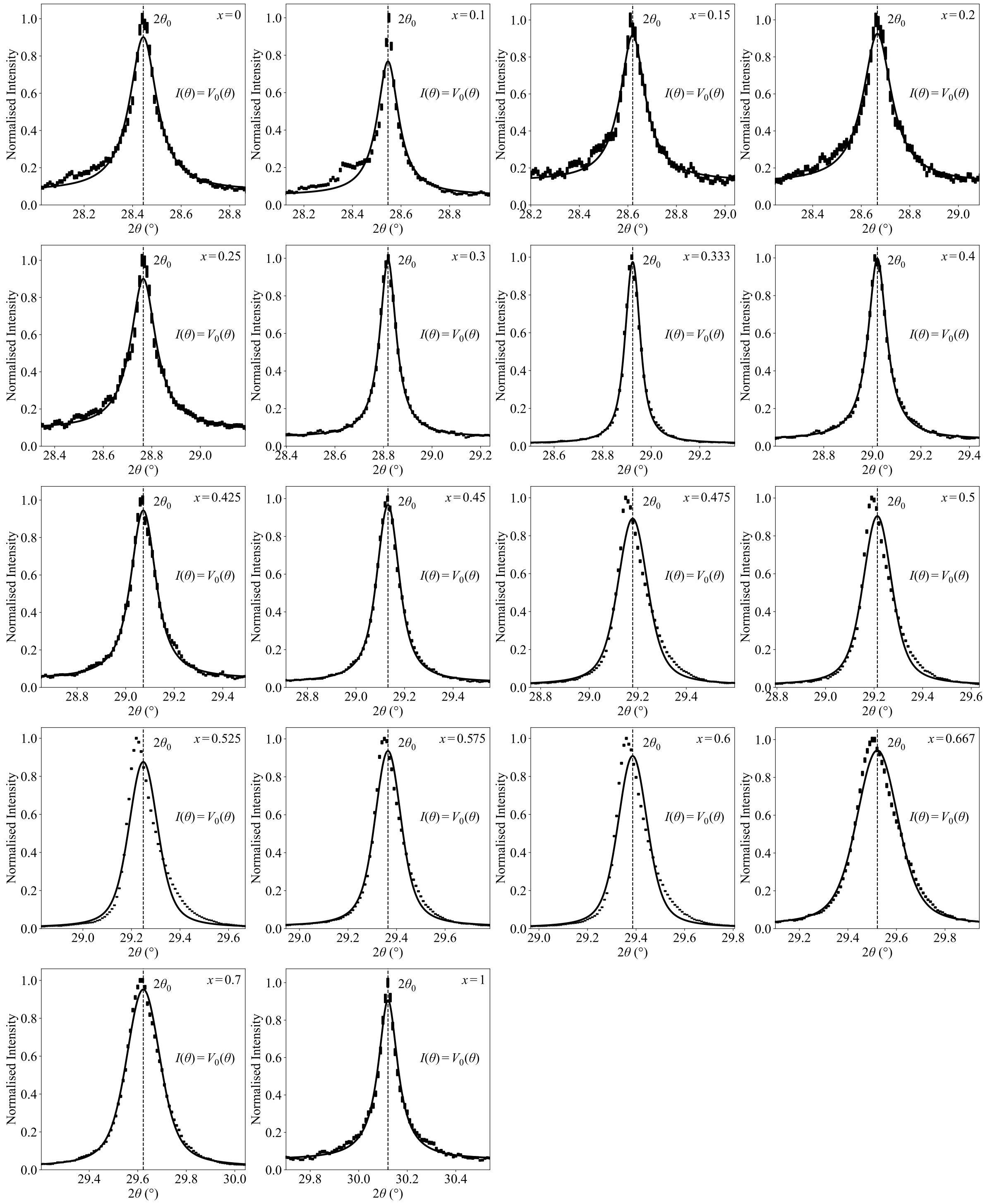

Figure S17. Second-order diffraction peak for MAPb(I$_{1-x}$Br$_x$)$_3$ thin films (different set of samples to those shown in Figure S4 and Figure S19, evidencing reproducibility) recorded on a different diffractometer (here, Rigaku SmartLab) – the same trend is observed as in Figure S4. Films were encapsulated with PMMA. Diffraction patterns were recorded using monochromatic Cu-Kα_1 radiation. The nominal bromide fraction is indicated in the upper-right of each individual plot. Data is modelled with a single Voigt profile. The dashed line indicates the peak centre extracted from the fit, and is marked as $2\theta_0$.

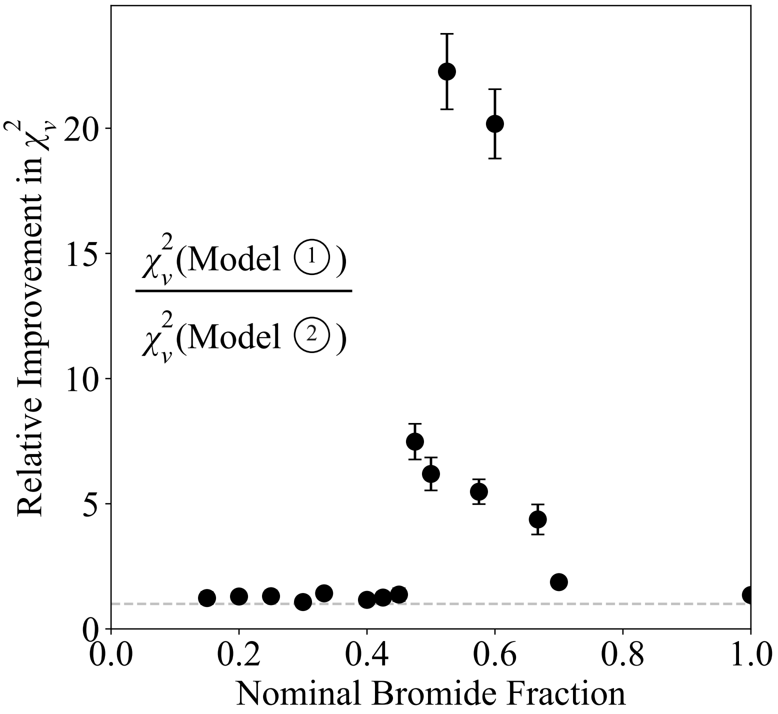

Figure S18. Ratio of the minimised reduced χ^2 (χ_v^2) when moving from the use of a single Voigt profile to the use of the sum of two Voigt profiles to model the (200) diffraction peak for $MAPb(I_{1-x}Br_x)_3$ thin-film samples on z-cut quartz presented in Figure S17. Compositions that crystallised into the tetragonal phase (i.e., $x = 0$ and $x = 0.1$) have been omitted.

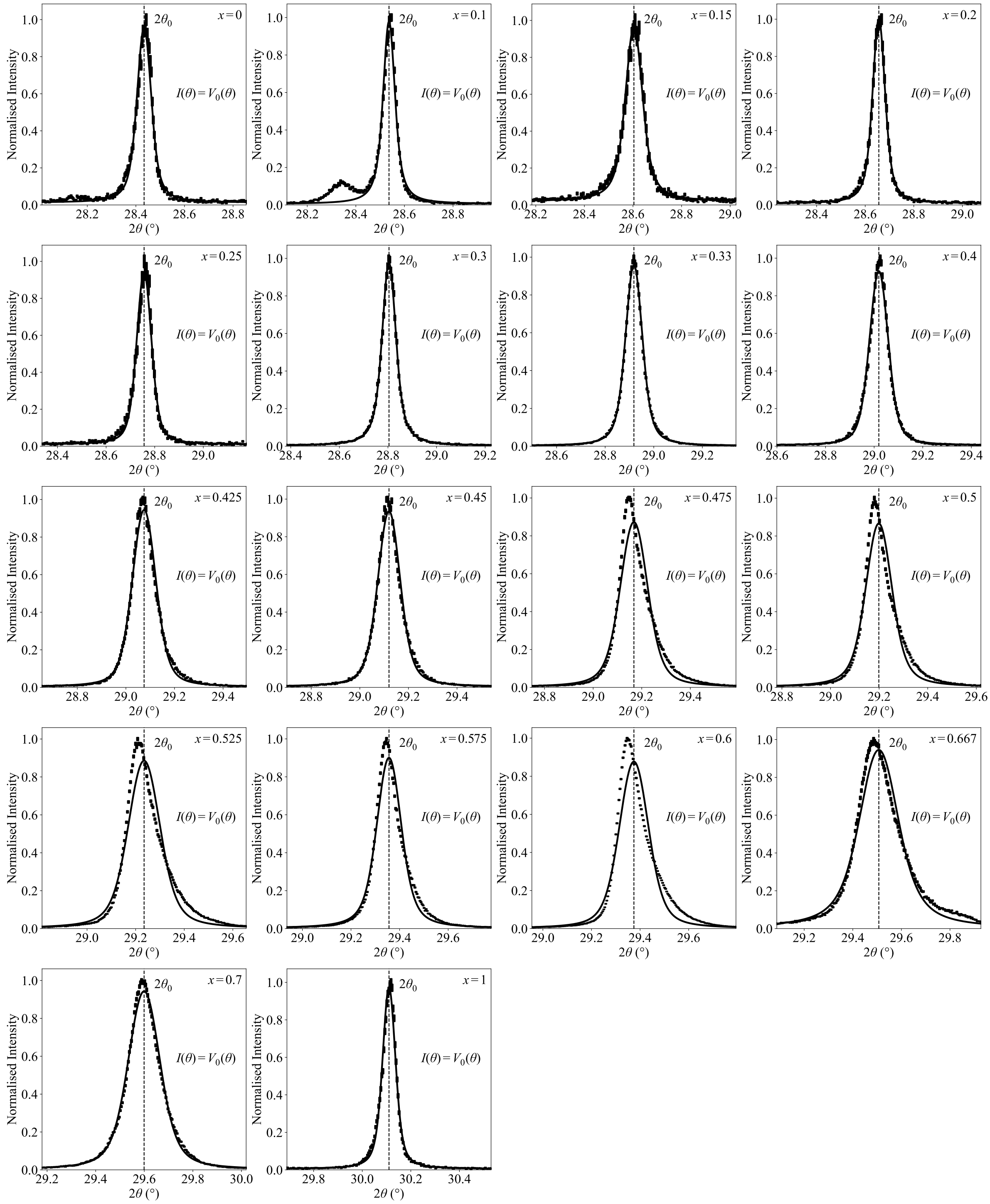

Figure S19. Second-order diffraction peak for MAPb($I_{1-x}Br_x$)$_3$ thin films with PMMA encapsulant (different set of samples to those shown in Figure S4 and Figure S17, evidencing reproducibility) – the same trend is observed as in Figure S4. Diffraction patterns were recorded using monochromatic Cu-Kα_1 radiation. The nominal bromide fraction is indicated in the upper-right of each individual plot. Data is modelled with a single Voigt profile. The dashed line indicates the extracted peak centre from the fit, and is marked as $2\theta_0$.

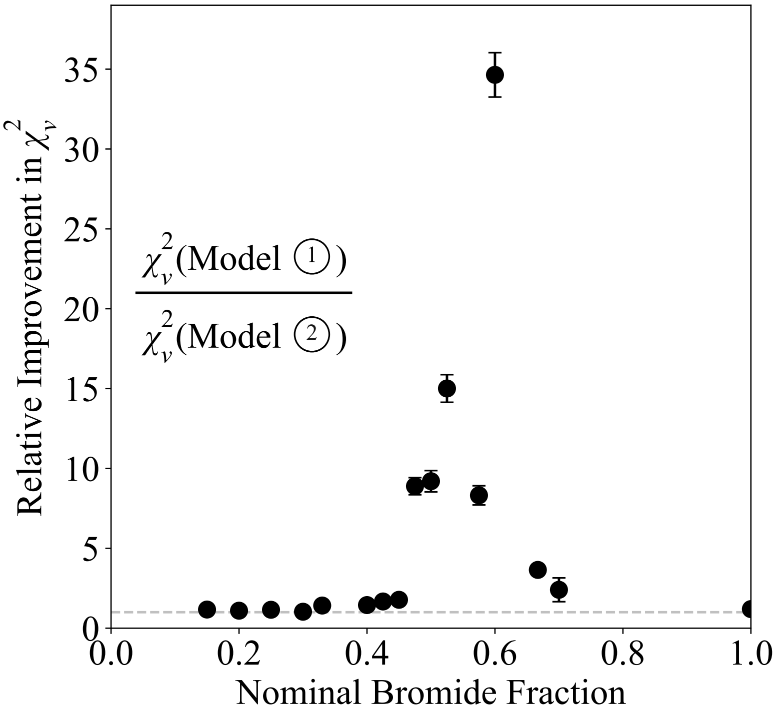

Figure S20. Ratio of the minimised reduced χ^2 (χ_v^2) when moving from the use of a single Voigt profile to the use of the sum of two Voigt profiles to model the (200) diffraction peak for MAPb($I_{1-x}Br_x$)$_3$ thin-film samples on z-cut quartz presented in Figure S19. Compositions that crystallised into the tetragonal phase (i.e., $x = 0$ and $x = 0.1$) have been omitted.

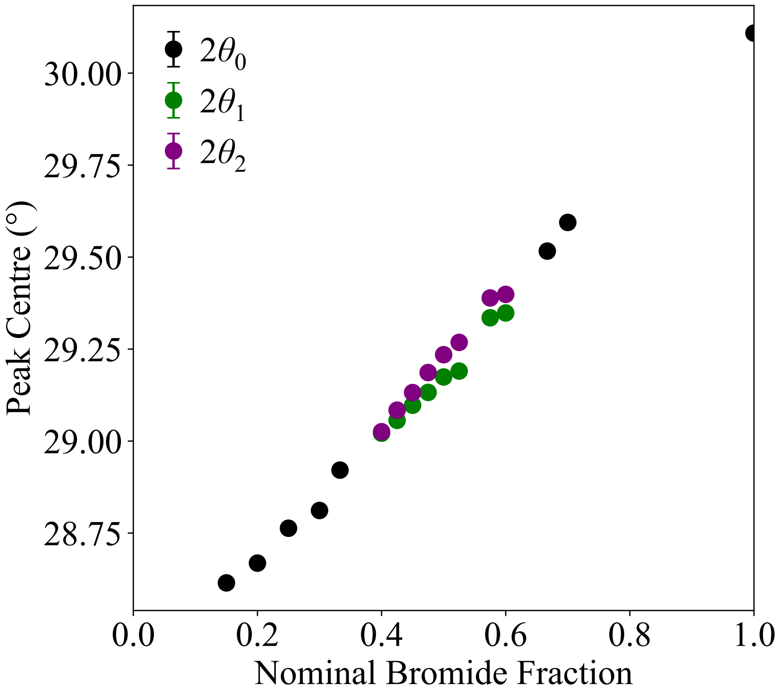

Figure S21. Centres of second-order X-ray diffraction peaks for $MAPb(I_{1-x}Br_x)_3$ thin films, extracted from modelling with a single Voigt profile (black) and the sum of two Voigt profiles (green and purple), and displayed over the appropriate range (Figure 1d and Figure 1e). Data extracted from Figure S4 and Figure S9. Compositions that crystallised into the tetragonal phase (i.e., $x = 0$ and $x = 0.1$) have been omitted.

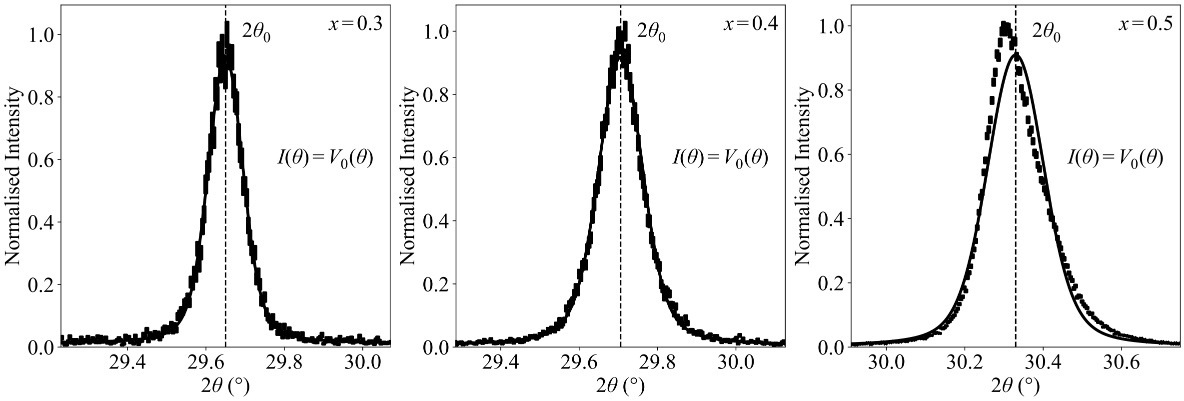

Figure S22. Second-order diffraction peak for $MAPb(I_{1-x}Br_x)_3$ thin films prepared as part of a separate batch – the same trend is observed as in Figure S4. This was the first batch fabricated, and used a shorter annealing time of 60 min. Compared to when a 90 min annealing time was used (Figure S16), no meaningful change in peak shape is observed: the asymmetry is still present for the composition with x equal to 0.5, even after an additional annealing of 30 min, indicating that different annealing times do not alter our findings. For the second batch of samples (where we targeted 22 different compositions, and forms the basis of this paper), we continued to use a 90 min annealing time. Films were encapsulated. Diffraction patterns were recorded using monochromatic Cu-Kα_1 radiation. The nominal bromide fraction is indicated in the upper-right of each individual plot. Data is modelled with a single Voigt profile. The dashed line indicates the peak centre extracted from the fit, and is marked as $2\theta_0$.

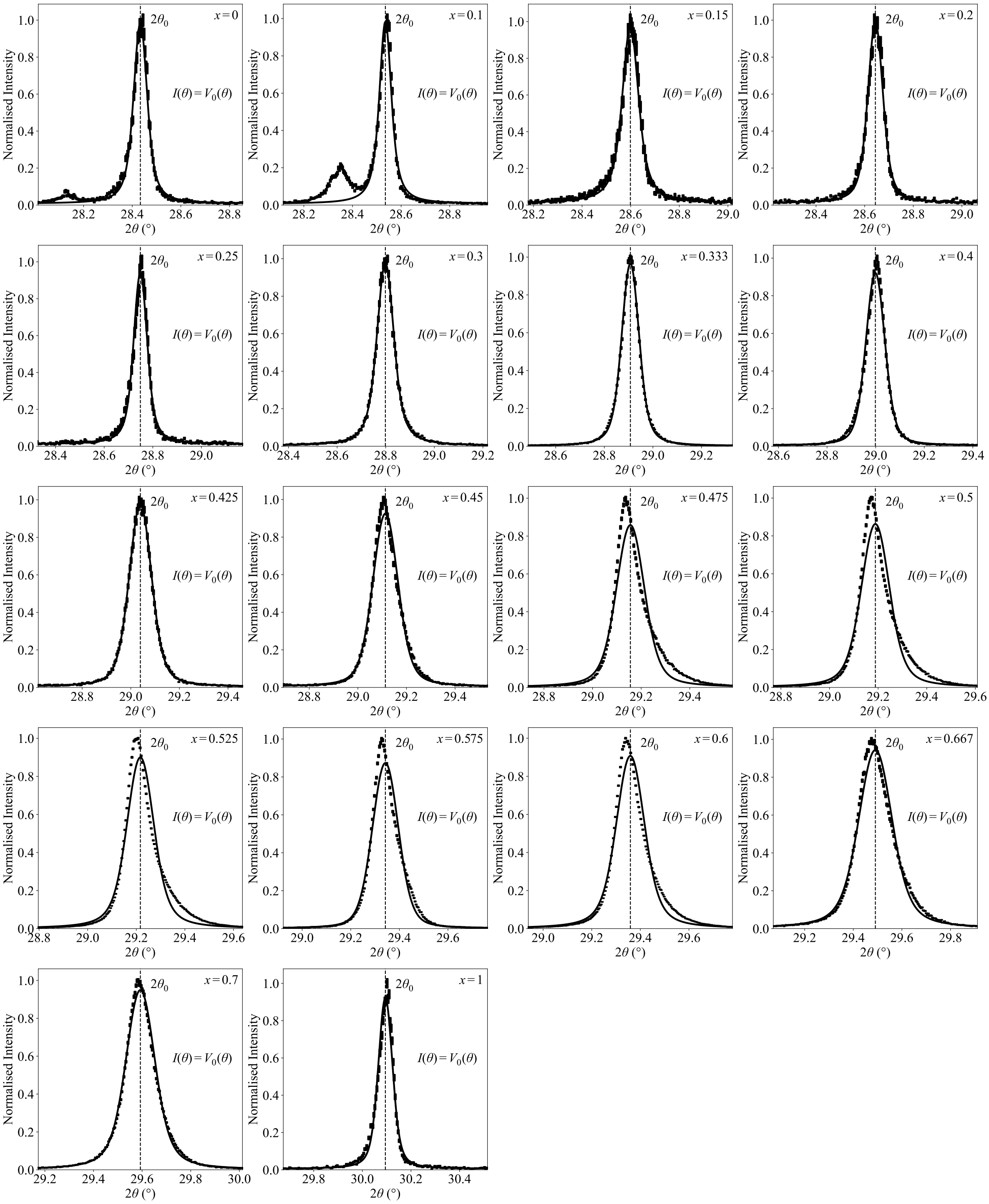

Figure S23. Second-order diffraction peak for $MAPb(I_{1-x}Br_x)_3$ thin films that had previously been exposed to continuous light-soaking (16 h for mixed-halide compositions, 2 h for pure halide compositions) and then had been allowed to remix in the dark over approximately 45 days – the same trend is observed as in Figure S4. Films were encapsulated with PMMA. Diffraction patterns were recorded using monochromatic Cu-Kα_1 radiation. The nominal bromide fraction is indicated in the upper-right of each individual plot. Data is modelled with a single Voigt profile. The dashed line indicates the peak centre extracted from the fit, and is marked as $2\theta_0$.

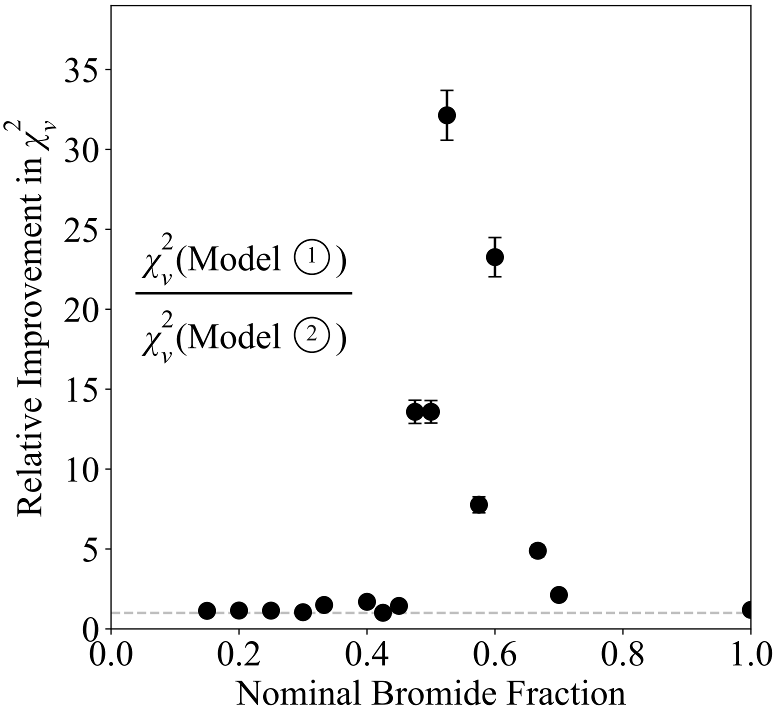

Figure S24. Ratio of the minimised reduced χ^2 (χ_v^2) when moving from the use of a single Voigt profile to the use of the sum of two Voigt profiles to model the (200) diffraction peak for MAPb($I_{1-x}Br_x$)$_3$ thin-film samples on z-cut quartz presented in Figure S23. Compositions that crystallised into the tetragonal phase (i.e., $x = 0$ and $x = 0.1$) have been omitted.

Supporting Note 2: Experimental design

Whilst mixed A-site cation MHPs have exhibited enhanced performance/stability, previous research suggests that halide segregation can be triggered by A-site cation segregation.[23] Consequently, to isolate the effects of halide segregation, we have utilised a single A-cation stoichiometry. The influence of the atmospheric environment has been demonstrated to strongly impact halide segregation dynamics.[5] To negate any atmospheric effects, all samples involved in segregation studies were coated in PMMA encapsulant. The films presented in Figure 1 (a study of the material structure prior to any illumination/segregation) were not coated in PMMA encapsulant to avoid the PMMA interacting with the perovskite structure below, and thus ensuring that any asymmetry present was not due to the encapsulating layer. As Figure S19 and S20 show, films encapsulated with PMMA were later found to exhibit the same trend as unencapsulated films (Figure S4 and Figure 1d) showing that the presence of a PMMA top layer does not affect our findings. Previous work has highlighted how X-ray exposure can induce material degradation and influence segregation dynamics.[24] Cumulative X-ray dosage was limited by utilising a lab-based diffractometer (i.e., not synchrotron based) equipped with a crystal monochromator. Finally, segregation dynamics have also been demonstrated to be strongly dependent on the fraction of charge carriers undergoing trap-mediated recombination.[5] As the bimolecular recombination rate has been shown not to be constant with varying halide fraction,[25] we excite in the low-intensity regime to minimise any differences in recombination pathway preferences between compositions. Illumination is provided by a continuous wave laser of 470 nm wavelength, with an intensity of 0.91 mWcm^{-2}. Using a relatively low illumination intensity sufficiently slows segregation, such that longer X-ray diffraction signal acquisition periods can be utilised without suffering from temporal smearing, improving the relative measurement signal-to-noise.

Supporting Note 3: Calculating the relative structural change

As a quasi-continuous spectrum of compositionally dissimilar regions of material are formed during segregation (each with possibly independent strain and particle size distributions), direct modelling of the diffraction profile was not deemed suitable. Instead, we quantify the impact of segregation via evaluation of the relative structural change. The relative structural change is calculated by taking the absolute integral of the differential intensity (for the relevant diffraction peak(s)), and normalising this value with respect to the time-zero peak integral (i.e., before illumination). This metric provides a measure of the relative proportion of material that has exhibited a change in lattice parameter, and hence is indicative of the volume of bromide/iodide-rich regions forming due to halide segregation. Crystallite fracturing, and the structure form factor could both artificially alter the calculated value of the relative structural change; however, previous research has evidenced that such effects are expected to be negligible compared to the structural change associated with the ionic redistribution of halides during phase segregation.[23,26,27] Possible material degradation or beam intensity changes during the experiment are accounted for by subtracting any change in the total peak area with time (generally observed to be negligible, see Figure S11). Variation in the diffraction signal-to-noise ratio between different compositions will further induce a base-line shift as an absolute integral is being calculated; this shift was corrected for by modelling the signal with Poisson statistics.

Mathematically, the relative structural change (RSC) at time *t* can be described as:

$$\begin{aligned}\mathrm{RSC}(t) &= \left(\frac{\int |I(t,2\theta) - I(t=0,2\theta)|\mathrm{d}2\theta}{\int I(t=0,2\theta)\mathrm{d}2\theta} - \frac{|\int I(t,2\theta) - I(t=0,2\theta)\mathrm{d}2\theta|}{\int I(t=0,2\theta)\mathrm{d}2\theta}\right) \\ &\quad - \left(\frac{\int |I(t,2\theta) - I'(t,2\theta)|\mathrm{d}2\theta}{\int I(t=0,2\theta)\mathrm{d}2\theta} - \frac{|\int I(t,2\theta) - I'(t,2\theta)\mathrm{d}2\theta|}{\int I(t=0,2\theta)\mathrm{d}2\theta}\right) \\ &= (A - B) - (C - D),\end{aligned} \tag{1}$$

where *I* is the measured XRD intensity at an angle 2θ and time *t,* and *A*, *B*, *C*, and *D* are defined to allow for later referral to each of the terms in Eq. 1. *I'* is a synthetic XRD pattern that is generated by utilising a Poisson sample as such:

$$I'_n = \mathrm{Poisson}\left(\frac{\sum_{n+1}^{n+5} I_n + \sum_{n-5}^{n-1} I_n}{10}\right) \tag{2}$$

where n is the n^{th} recorded XRD pattern (evenly spaced, with a total of N recorded XRD patterns). All integrals are evaluated between 27.5 ° and 31 ° (see Section 5).

We will now consider each of the four terms described in Eq. 1. The first term (A) calculates the absolute change in the second-order peak with respect to the time-zero peak (grey shading, Figure S25). The second term (B) corrects for any material degradation (possible peak area loss) that is not associated with halide segregation, or any change in X-ray flux during the experiment. The third (C) and fourth (D) term (copying the structure of the first two terms) correct for the noise that is integrated in A and B (we are taking an absolute integral, so normally distributed noise will no longer sum to zero – see signal far from the peak in Figure S25). D will effectively always go to zero, but is included to ensure mathematical consistency. As I' is calculated via a ten-point effective rolling average (used to obtain a low-noise estimate from which to take the Poisson sample), there are ten time steps that do not have a correction directly calculated. C and D are set to zero for the initial ($t = 0$) time step, are taken as an average of time steps six through ten to fill in the second through fifth time step, and are taken as an average of the $(N - 9)^{\text{th}}$ through to the $(N - 5)^{\text{th}}$ time step for the final five points. Example relative structural change traces, showing the correction procedure, are presented for a non-segregating material ($x = 0$) in Figure S26, and a segregating material ($x = 0.3$) in Figure S27.

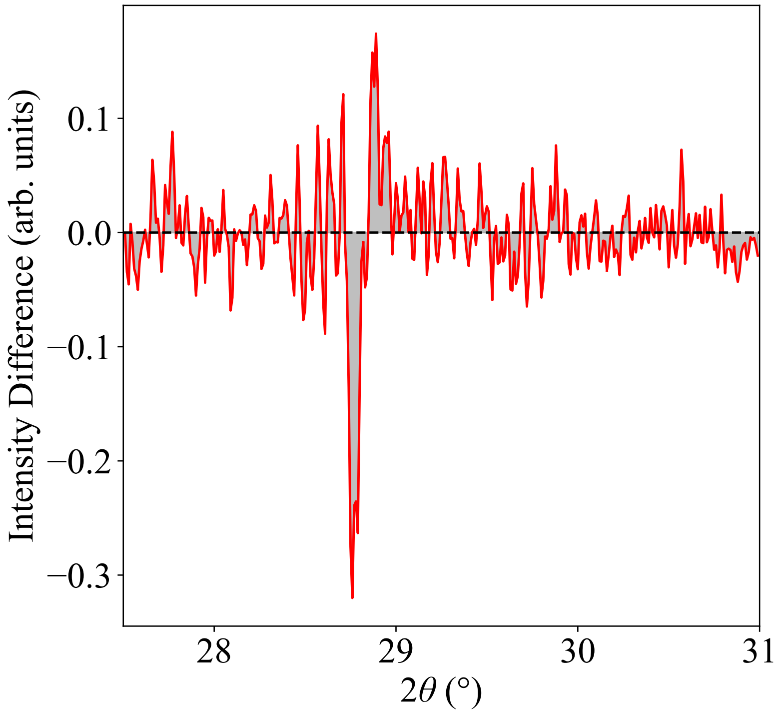

Figure S25. Intensity difference for the (200) diffraction peak after 16 h of continuous illumination (with respect to the peak obtained before illumination) for a composition with a nominal bromide fraction of 0.25. Note that for this method implementing integration over absolute signal values, the noise will be absolutely integrated far away from the peak signal and therefore requires the corrections described above and illustrated in Figures S26 & S27 below.

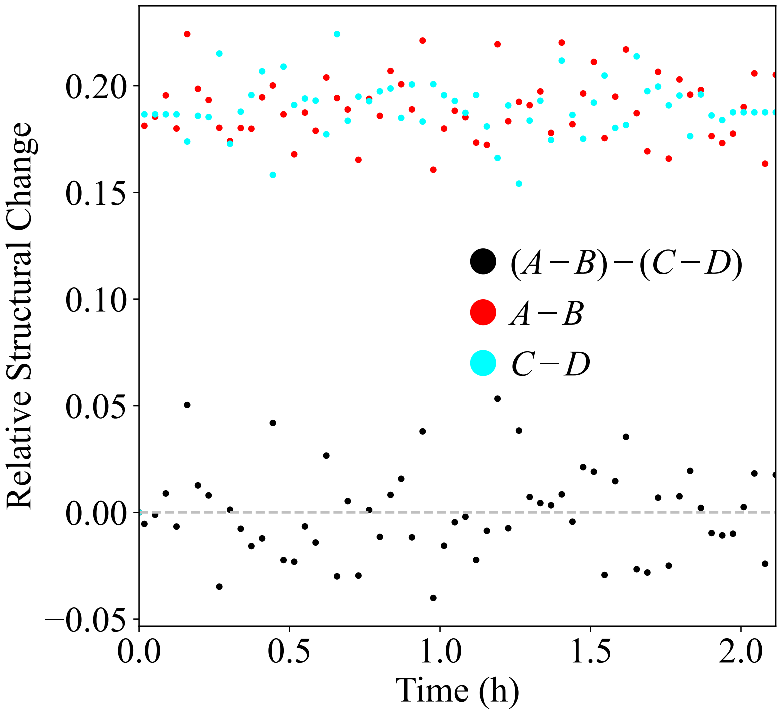

Figure S26. Example correction procedure for the relative structural change as a function of illumination time for a composition with a nominal bromide fraction of 0. For this single-halide composition, there will be no segregation, and thus, the relative structural change should be effectively zero. This is exactly what application of the correction method achieves.

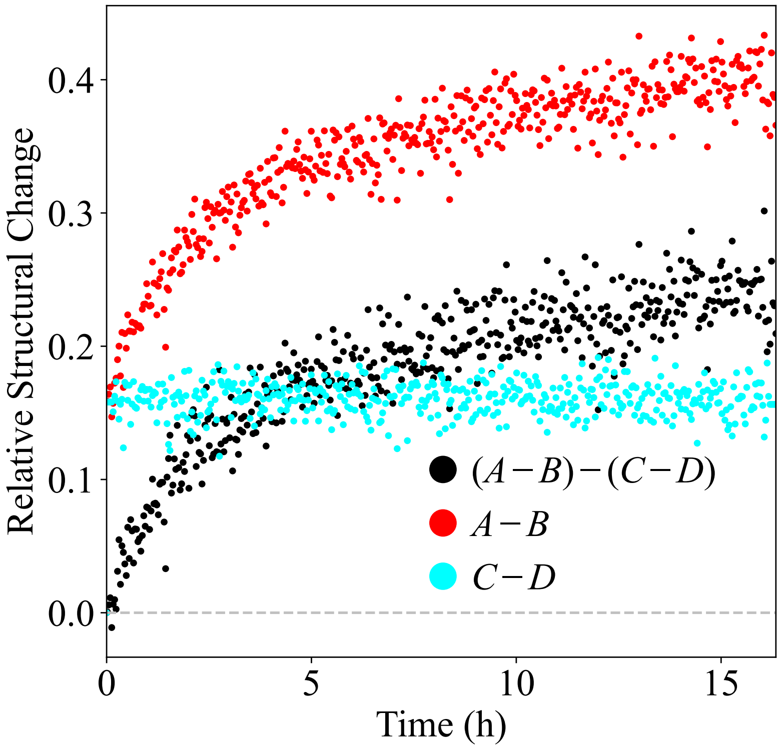

Figure S27. Example correction procedure for the relative structural change as a function of illumination time for a MAPb($I_{1-x}Br_x$)$_3$ composition with a nominal bromide fraction of 0.3. For this mixed-halide composition, we see that the correction procedure is able to suitably correct for the noise-induced offset.

Supporting Note 4: Extracting average rate of structural change

As we show in the main text (Figure 2g), while some compositions show halide segregation dynamics compatible with monoexponential rise functions, others exhibited a biexponential dynamic. In order to obtain representative average rise rates across the whole compositional space, we therefore implemented a simple metric associated with the time taken for the relative structural change signal to reach 63% of the final 'saturated' value, using a phenomenological fitting function for the purpose of accuracy (Figure S28 illustrates this process). For this purpose, the lower- and upper-bound relative structural change traces (i.e., computed values minus standard errors, and computed values plus standard errors) were fitted with a sixth-order polynomial (no constant term), and the intercepts of these polynomials with the numerical rise time (time taken to reach 63% of the final 'saturated' value) were taken as the bounds for the estimated characteristic rise time. The estimated characteristic rise time was taken as the midpoint of these bounds, with the bounds defining the uncertainty in the estimated rise time value. An estimated rate (Figure 2f) was then calculated by taking the inverse of the estimated rise time. Due to a low measurement signal-to-noise (Figure S12), estimated rates could not be computed for the $x = 0.15$ or $x = 0.25$ compositions (Figure 2f) which show very little amplitude of halide segregation.

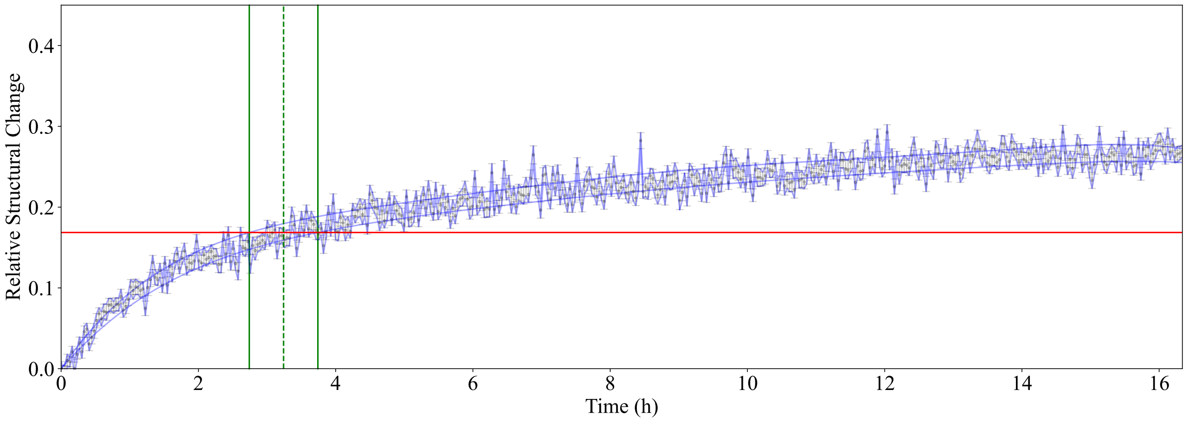

Figure S28. Example relative structural change trace (black) for a $MAPb(I_{1-x}Br_x)_3$ thin film with a nominal bromide fraction of 0.5. Lower- and upper-bound traces (blue) were fitted with a sixth-order polynomial (no constant term). The intercepts of these polynomials with the numerical rise time (red) were taken as the bounds (green, solid) for the estimated characteristic rise time. The estimated characteristic rise time was taken as the midpoint (green, dashed) of these bounds, with the bounds (green, solid) defining the uncertainty in the estimated rise time value.

References

[1] J. B. Patel, R. L. Milot, A. D. Wright, L. M. Herz, M. B. Johnston, Formation Dynamics of CH3NH3PbI3 Perovskite Following Two-Step Layer Deposition, *J. Phys. Chem. Lett.* **2016**, *7*, 96.

[2] G. Jovanovski, T. Šijakova-Ivanova, I. Boev, B. Boev, P. Makreski, Intriguing Minerals: Quartz and Its Polymorphic Modifications, *ChemTexts* **2022**, *8*, 14.

[3] C. C. Stoumpos, C. D. Malliakas, M. G. Kanatzidis, Semiconducting Tin and Lead Iodide Perovskites with Organic Cations: Phase Transitions, High Mobilities, and Near-Infrared Photoluminescent Properties, *Inorg. Chem.* **2013**, *52*, 9019.

[4] F. C. Hanusch, E. Wiesenmayer, E. Mankel, A. Binek, P. Angloher, C. Fraunhofer, N. Giesbrecht, J. M. Feckl, W. Jaegermann, D. Johrendt, T. Bein, P. Docampo, Efficient Planar Heterojunction Perovskite Solar Cells Based on Formamidinium Lead Bromide, *J. Phys. Chem. Lett.* **2014**, *5*, 2791.

[5] A. J. Knight, A. D. Wright, J. B. Patel, D. P. McMeekin, H. J. Snaith, M. B. Johnston, L. M. Herz, Electronic Traps and Phase Segregation in Lead Mixed-Halide Perovskite, *ACS Energy Lett.* **2019**, *4*, 75.

[6] J. H. Noh, S. H. Im, J. H. Heo, T. N. Mandal, S. I. Seok, Chemical Management for Colorful, Efficient, and Stable Inorganic–Organic Hybrid Nanostructured Solar Cells, *Nano Lett.* **2013**, *13*, 1764.

[7] M. C. Brennan, A. Ruth, P. V. Kamat, M. Kuno, Photoinduced Anion Segregation in Mixed Halide Perovskites, *Trends Chem.* **2020**, *2*, 282.

[8] V. J.-Y. Lim, A. J. Knight, R. D. J. Oliver, H. J. Snaith, M. B. Johnston, L. M. Herz, Impact of Hole-Transport Layer and Interface Passivation on Halide Segregation in Mixed-Halide Perovskites, *Adv. Funct. Mater.* **2022**, *32*, 2204825.

[9] R. W. Cheary, A. A. Coelho, Axial Divergence in a Conventional X-Ray Powder Diffractometer. I. Theoretical Foundations, *J. Appl. Crystallogr.* **1998**, *31*, 851.

[10] L. W. Finger, D. E. Cox, A. P. Jephcoat, A Correction for Powder Diffraction Peak Asymmetry Due to Axial Divergence, *J. Appl. Crystallogr.* **1994**, *27*, 892.

[11] W. L. Tan, C. R. McNeill, X-Ray Diffraction of Photovoltaic Perovskites: Principles and Applications, *Appl. Phys. Rev.* **2022**, *9*, 021310.

[12] C. Rehermann, A. Merdasa, K. Suchan, V. Schröder, F. Mathies, E. L. Unger, Origin of Ionic Inhomogeneity in MAPb(IxBr1–x)3 Perovskite Thin Films Revealed by In-Situ Spectroscopy during Spin Coating and Annealing, *ACS Appl. Mater. Interfaces* **2020**, *12*, 30343.

[13] D. W. deQuilettes, J. J. Yoo, R. Brenes, F. U. Kosasih, M. Laitz, B. D. Dou, D. J. Graham, K. Ho, Y. Shi, S. S. Shin, C. Ducati, M. G. Bawendi, V. Bulović, Reduced Recombination via Tunable Surface Fields in Perovskite Thin Films, *Nat. Energy* **2024**, *9*, 457.

[14] Q. Jiang, J. Tong, R. A. Scheidt, X. Wang, A. E. Louks, Y. Xian, R. Tirawat, A. F. Palmstrom, M. P. Hautzinger, S. P. Harvey, S. Johnston, L. T. Schelhas, B. W. Larson, E. L. Warren, M. C. Beard, J. J. Berry, Y. Yan, K. Zhu, Compositional Texture Engineering for Highly Stable Wide-Bandgap Perovskite Solar Cells, *Science* **2022**, *378*, 1295.

[15] T. Elmelund, R. A. Scheidt, B. Seger, P. V. Kamat, Bidirectional Halide Ion Exchange in Paired Lead Halide Perovskite Films with Thermal Activation, *ACS Energy Lett.* **2019**, *4*, 1961.

[16] P. Shi, J. Xu, I. Yavuz, T. Huang, S. Tan, K. Zhao, X. Zhang, Y. Tian, S. Wang, W. Fan, Y. Li, D. Jin, X. Yu, C. Wang, X. Gao, Z. Chen, E. Shi, X. Chen, D. Yang, J. Xue, Y. Yang, R. Wang, Strain Regulates the Photovoltaic Performance of Thick-Film Perovskites, *Nat. Commun.* **2024**, *15*, 2579.

[17] T. Soto-Montero, W. Soltanpoor, M. Morales-Masis, Pressing Challenges of Halide Perovskite Thin Film Growth, *APL Mater.* **2020**, *8*, 110903.

[18] C. Lin, A. Z. Li, The Effect of Strain on the Miscibility Gap in Ga–In–Sb Ternary Alloy, *J. Cryst. Growth* **1999**, *203*, 511.

[19] J. E. Lee, M. Righetto, B. W. J. Putland, S. Yan, J. R. S. Lilly, S. Lal, H. Jin, N. K. Noel, M. B. Johnston, H. J. Snaith, L. M. Herz, Impact of Charge Transport Layers on the Structural and Optoelectronic Properties of Coevaporated Cu2AgBiI6, *ACS Appl. Mater. Interfaces* **2025**, *17*, 40363.

[20] S. Yan, J. B. Patel, J. E. Lee, K. A. Elmestekawy, S. R. Ratnasingham, Q. Yuan, L. M. Herz, N. K. Noel, M. B. Johnston, A Templating Approach to Controlling the Growth of Coevaporated Halide Perovskites, *ACS Energy Lett.* **2023**, *8*, 4008.

[21] W. Li, M. Hao, A. Baktash, L. Wang, J. Etheridge, The Role of Ion Migration, Octahedral Tilt, and the A-Site Cation on the Instability of Cs1-xFAxPbI3, *Nat. Commun.* **2023**, *14*, 8523.

[22] H. Funk, O. Shargaieva, A. Eljarrat, E. L. Unger, C. T. Koch, D. Abou-Ras, In Situ TEM Monitoring of Phase-Segregation in Inorganic Mixed Halide Perovskite, *J. Phys. Chem. Lett.* **2020**, *11*, 4945.

[23] A. J. Knight, J. Borchert, R. D. J. Oliver, J. B. Patel, P. G. Radaelli, H. J. Snaith, M. B. Johnston, L. M. Herz, Halide Segregation in Mixed-Halide Perovskites: Influence of A-Site Cations, *ACS Energy Lett.* **2021**, *6*, 799.

[24] M. E. Stuckelberger, T. Nietzold, B. M. West, Y. Luo, X. Li, J. Werner, B. Niesen, C. Ballif, V. Rose, D. P. Fenning, M. I. Bertoni, Effects of X-Rays on Perovskite Solar Cells, *J. Phys. Chem. C* **2020**, *124*, 17949.

[25] J. E. Lee, S. G. Motti, R. D. J. Oliver, S. Yan, H. J. Snaith, M. B. Johnston, L. M. Herz, Unraveling Loss Mechanisms Arising from Energy-Level Misalignment between Metal Halide Perovskites and Hole Transport Layers, *Adv. Funct. Mater.* **2024**, *34*, 2401052.

[26] C. G. Bischak, C. L. Hetherington, H. Wu, S. Aloni, D. F. Ogletree, D. T. Limmer, N. S. Ginsberg, Origin of Reversible Photoinduced Phase Separation in Hybrid Perovskites, *Nano Lett.* **2017**, *17*, 1028.

[27] K. Suchan, Life and Death of Mixed Metal Halide Perovskites, Lund University, **2023**.